Condensation and wicking of water on solid nanopatterns

Jae Hong Lee,[1] Buyoung Jung,[2] Gui-su Park,[2] and Ho-Young Kim ●[1,*]

[1]*Department of Mechanical Engineering, Seoul National University, Seoul 08826, Korea*
[2]*Semes Co. Ltd., Cheonan-si, Chungcheongnam-do 31040, Korea*

Although liquid behaviors in micrometric scales can be observed optically and those below nanometric scales can be probed with atomic force microscopy, those in the ranges from tens to hundreds of nanometers have seldom been visualized due to limits in optical and electron microscopy. Here we report direct visualization of condensation and wicking of water on arrays of solid walls with gaps ranging from tens to hundreds of nanometers, by reducing electron-beam-induced heating in the environmental scanning electron microscopy. We find that the water condensing and wicking on hydrophilic nanopatterns exhibits little difference from what has been observed on micropatterns. However, the condensation behavior of water on hydrophobic nanopatterns is found not to follow the conventional capillary condensation theory. The hydrophobic grooves of 40–80 nm widths are observed to be completely wetted by condensing water vapor, but do not allow externally approaching liquid water to invade themselves. We expect our experiments to trigger further experimental attempts to observe nanoscale liquid menisci in various situations. In addition, those peculiar nanoscale behaviors of water reported here will broaden our knowledge of nanoscale wetting and feed empirical inputs for theoretical models.

I. INTRODUCTION

Understanding and controlling the static and dynamic behavior of nanoscale liquid-gas menisci on solids are important in a range of biological and artificial settings. For example, nanoscale water menisci around stomata in plant leaves are responsible for the negative pressure, or tension, in water that drives sap flow through a plant [1]. Wet etching and cleaning of very-large-scale integrated semiconductor chips critically rely on the movement of the meniscus of wet chemicals and cleansing solutions within nanoscale gaps [2]. Harvesting water from humid air resorts to heterogeneous condensation [3,4] or adsorption [5] of water on wettable surfaces, which involve generation of nanoscale water menisci.

It is well known that conventional optical microscopes cannot resolve distances smaller than a few hundred nanometers due to Abbe's diffraction limit [6]. While the scanning near-field optical microscope now beats the limit to observe tiny objects, tens of nanometers in size at visible wavelengths [7–9], it has failed to see a nanoscale liquid meniscus because a few tens of nanometer spacing between the lens and the liquid surface can induce capillary condensation or deform the liquid meniscus. Hence, electron microscopy has been used to observe nanoscale menisci thus far. The high-vacuum requirements of the scanning electron microscopy (SEM), which are detrimental to liquid, were circumvented by solidifying liquids before observation [10–12]. In transmission electron microscopy (TEM), liquids are encapsulated in closed-end carbon nanotubes [13,14] or in a liquid cell [15]. The environmental SEM (ESEM) has succeeded in seeing the microscale liquid
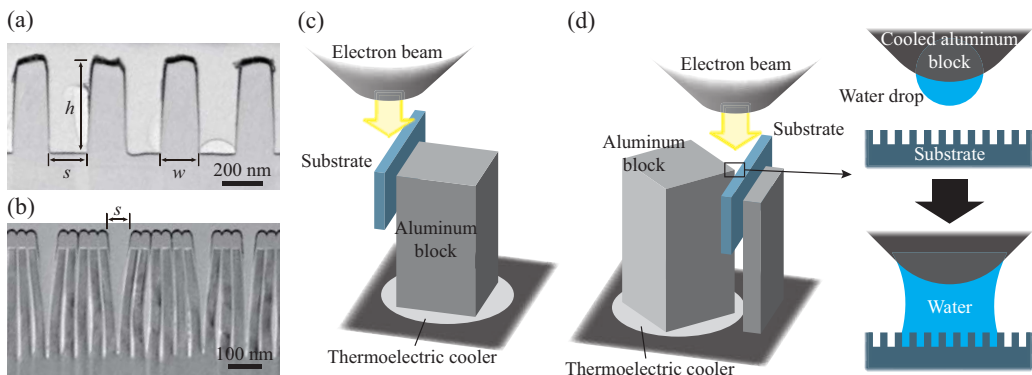
---

*hyk@snu.ac.kr

FIG. 1. (a) TEM image of the silicon patterns with width $w = 180$ nm, gap spacing $s = 180$ nm, and height $h = 400$ nm (surface type L). (b) TEM image of the silicon patterns with width $w = 25$ nm, gap spacing $s = 14$ nm, and height $h = 400$ nm (surface type S). (c) Schematic of the experimental setup in an ESEM chamber for condensation experiments. (d) Schematic of the experimental setup in an ESEM chamber for the wicking experiments. Water vapor condenses at the vertex of the aluminum block in contact with the thermoelectric cooler. The water drop grows toward the nanopatterned substrate. When the drop contacts the substrate making a millimetric liquid bridge, the contact behavior of the drop with the substrate can be observed by the electron beam

meniscus without encapsulation due to its capability of stable visualization with an electron beam at high pressure up to tens of millibars. By lowering the temperature below the dew point of the water vapor in the ESEM chamber, condensed water microdrops were visualized on solid [16] and oil [17] surfaces.

However, the visualization of nanoscale water menisci without solidification or encapsulation has been very difficult because of the intense heating of the sample by an electron beam at high magnification [18,19]. Atomic force microscopy (AFM) was used to probe water menisci a few nanometers in size, but it takes a significantly long time to probe larger menisci with AFM [20–22]. Thus, directly visualizing water menisci in ranges from tens to hundreds of nanometers has remained rather unexplored. Here we report direct visualization results of the water menisci formed on nanopatterned solid surfaces. This is achieved through ESEM by devising ways to reduce the heating effects of the electron beam. We go beyond observation of mere condensation of water on solids by further visualizing the meniscus dynamics upon contact with an external microdrop with nanoscale solid patterns.

In the following, we first delineate the experimental procedures to visualize the nanoscale water menisci in the ESEM chamber. Then we present the experimentally observed condensation and wicking behaviors of nanoscale menisci on solid patterns with different dimensions and wetta-bilities, and theoretically analyze the results. Our results allow us to identify the similarities and differences of nanoscale and microscale water menisci on solids, which have been elusive for the lack of direct visual evidence.

II. EXPERIMENT

As solid surfaces, we employ two types of nanowall arrays that have been formed by reactive ion etching of Si wafers. The type L surface has identical linewidth w and gap spacing s of 180 nm and a height h of 400 nm, as shown in Fig. 1(a). The type S surface comprises an array of walls with 25 nm width and 400 nm height. Although the nanowalls are apart from each other by 14 nm at the base, the actual spacing of wall heads indicated as s in Fig. 1(b) ranges from 40 to 80 nm because

TABLE I. Apparent as-placed static contact angles of water on the flat and patterned surfaces.

Surface	Flat surface	Surface L	Surface S
Platinum coated surface (I)	$42 \pm 1°$	$33 \pm 5°$	$32 \pm 6°$
PTFE coated surface (O)	$100 \pm 1°$	$104 \pm 7°$	$102 \pm 8°$

of elastocapillary clustering of the thin walls with evaporation of cleansing solution after etching [23,24]. Here L and S stand for large and small gaps, respectively.

To prepare hydrophilic surfaces causing no electric breakdown under an electron beam, we coat the surfaces with Pt via sputtering, yielding hydrophilic surfaces labeled LI and SI, with I standing for hydrophilic. To gain hydrophobicity, we coated the Si surfaces with polytetrafluoroethylene (PTFE) via dip coating in 10 wt. % PTFE solution of Fluorinert FC-40 (3M) and baking at 150 °C for 1 h. The hydrophobic surfaces are labeled LO and SO, with O representing hydrophobic. The apparent as-placed static contact angles θ_s of water on the surfaces are measured using sessile drops of 1 μl in volume. We list the measured values of θ_s on the flat and patterned surfaces in Table I. The standard deviations on the patterned surfaces are relatively large due to variation of θ_s depending on the viewing angle with respect to the line pattern direction.

We employ ESEM (FEI XL-30 FEG, Philips) to introduce water and observe its nanoscale liquid meniscus on solids. With water vapor supplied in the ESEM chamber, solid surfaces are cooled by a thermoelectric cooler to 2 °C, for which the saturation vapor pressure of water is 5.3 Torr (706.6 Pa). The water vapor pressure is initially supplied up to 4.5 Torr (600 Pa) and then maintained for 1–5 min. The condensation can be observed even before the saturation vapor pressure is reached, as will be described in next section. When no further condensation is observed, we increase the vapor pressure by 0.1 Torr (13.3 Pa). We repeat the observation and the vapor supply until reaching the saturation vapor pressure. We observe the water meniscus from the side, as well as on the top surface, of the nanoarrays.

A key technique in the observing nanoscale meniscus with ESEM is to reduce the electron-beam intensity, the irradiation time, and the consequent heating over an area of interest. It is because condensation is delayed or prevented at a spot under a high-intensity electron beam employed to enable high magnification. Thus, we start with a low magnification to irradiate the electron beam over a wide region, resulting in low intensity per area, and wait until condensation arises on the cold surface. Then we zoom in on the area of interest to see the nanoscale meniscus. Observing the meniscus from the side of the nanopattern helps to reduce the solid area exposed to the focal plane of the electron beam [19].

We also observe the wicking of a drop that is brought in contact with the initially dry array of nanowalls. We induce condensation of a water drop at a vertex of an aluminum block which is cooled below the dew point of water by the thermoelectric cooler in the ESEM chamber, as illustrated in Fig. 1(d). The growing drop eventually touches the array approximately 200 μm from the vertex.

III. CONDENSATION BEHAVIOR

We present ESEM images of the different types of nanoscale arrays that are wetted by condensing water in Fig. 2. We first discuss the water condensing behavior on hydrophilic substrates, as shown in Figs. 2(a) and 2(b). On both arrays LI [Fig. 2(a)] and SI [Fig. 2(b)], the condensation begins within the nanogaps rather than on top of the linear patterns. The early formation of a water meniscus in the nanogaps is attributed to the capillary condensation favored at concave sharp corners [25–27]. We see in the first panel of Fig. 2(a) that the water starts to condense in a nanogap when the relative humidity (RH), the ratio of the current vapor pressure to the saturation vapor pressure at 2 °C, is 91%. When RH reaches 94% in the second panel, all the gaps are filled with water, and no further condensation proceeds with the constant RH. When RH reaches 100%, drops appear and then grow

(a)

(b)

(c)

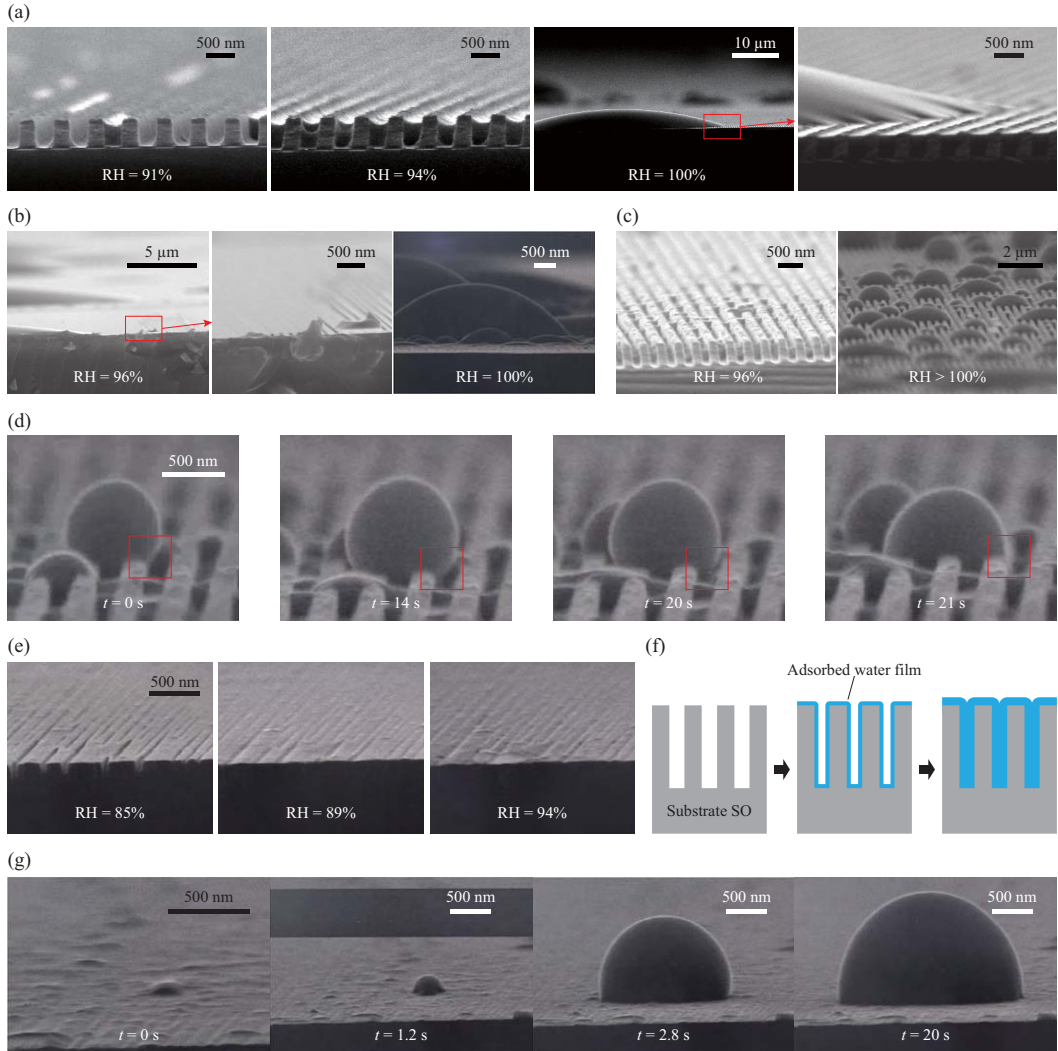

(d)

(e)

(f)

(g)

FIG. 2. Condensation of water on (a) surface *LI*, (b) surface *SI*, and (c) surface *LO*. (d) Drop spreading on the surface *LO*. (e) Condensation of water on the surface *SO*. (f) Schematic of the adsorption process of water on the surface *SO*. (g) Drop generation on the surface *SO*.

on top of the line patterns as shown in the third panel of Fig. 2(a). Wrinkles are visible on the drop interface, which extend approximately 1 μm from the contact line, in the fourth panel of Fig. 2(a). We suppose that the wrinkles evidence the interplay between the liquid's surface tension and the irregular intermolecular forces arising from the liquid's contact with the periodic solid patterns.

For hydrophilic patterns with finer gaps, surface type *SI* in Fig. 2(b), the narrow nanogaps are seen to be flooded before the saturation vapor pressure is reached. The condensation occurs so rapidly that the camera in the ESEM, which takes approximately 1 frame/s, cannot resolve the transient condensation behavior within the nanogaps. Drops appear on top of the line patterns flooded with water at RH of 96%, as shown in the first panel of Fig. 2(b). The drops continue to grow when RH reaches 100%, as seen in the third panel of Fig. 2(b).

On hydrophobic patterns with relatively large gaps, surface *LO*, condensation still occurs within the nanogaps, as shown in the first panel of Fig. 2(c). However, unlike what has been observed on

the hydrophilic patterns, liquid spots are sporadically distributed in the grooves without completely filling them. This indicates that the condensed water cannot infiltrate the hydrophobic grooves for the solid's relatively low surface energy. In addition, we can infer that the filled grooves on the aforementioned hydrophilic patterns are attributed to the capillary wicking as well as active capillary condensation at the groove corners. On the surface LO, the continued condensation at RH of 100% yields water drops on top of the line patterns instead of wicking along the grooves, as shown in the second panel of Fig. 2(c). Once formed, the drops provide a more facile venue for condensation on their own surfaces than on the hydrophobic solid surface. Thus, they keep growing while covering dry patterns, both crests and troughs, whose process is imaged in Fig. 2(d).

In Fig. 2(d) we observe the change of the apparent contact angle depending on the contact conditions of the contact line (shown in the red box). The contact angle is relatively large when the water-gas interface is about to get over the edge of the line pattern, as in the first three panels of Fig. 2(d). When the interface finally covers the top of the next pattern, the contact angle is reduced, as seen in the last panel. This behavior is similar to what has been observed for macroscale drops [28–30], indicating that the local pinning still plays an important role in determining the contact angle on the line patterns of approximately 100 nm spacing.

The water condensing behavior on hydrophobic patterns with finer gaps, surface SO, significantly differs from that on surface LO. The first two panels of Fig. 2(e) show that water condenses on top of the line patterns as well as in the grooves before RH reaches 90%. The third panel reveals that the entire grooves are filled with water while the pattern tops are also covered with a thin water film. The evolution of water film in this process is schematically illustrated in Fig. 2(f), suggesting that adsorption of water molecules is sufficient to fill the 40–80 nm wide grooves. The thickness of water film adsorbed on hydrophobic silica surfaces is known to be limited to less than 10 nm [31]. However, our water film is seen to exceed the thickness limit supposedly owing to narrow gap geometry that can restrict movements of vapor molecules. Compared to the multilayer adsorption that has been analyzed and reported in complete wetting situations [31–33], the formation mechanism of the thick adsorbed film as observed on the nanogaps of surface SO has been seldom reported, calling for future theoretical study.

The drop formation behavior on surface SO, as shown in Fig. 2(g), is also different from surface LO. At RH of 100%, a nanoscale bulge appears from a thin water film that covers the entire nanopattern and continues to grow to a microscale sessile drop. Although this drop is sitting on a water film, its contact angle of approximately $101°$ is comparable to the value of a macroscale drop on the dry hydrophobic surface. A speculation has been made recently that a nanoscopically thin liquid film exerts an insignificant effect on the contact angle of a sessile drop, based on indirect experimental observations, such as macroscale observation and theoretical analysis [34–36]. Figure 2(g) offers direct visual evidence for the speculation by showing both the nanofilm and microdrop.

IV. WICKING BEHAVIOR

Figure 3 shows the contact behavior of a liquid drop with nanopatterned surfaces of different wettabilities and dimensions. When a drop formed at a vertex of the adjacent aluminum block touches a hydrophilic pattern, the area surrounding the drop-solid contact region is also wetted by a liquid film, on both surfaces LI and SI, as shown in Figs. 3(a) and 3(b). Pattern tops as well as grooves are seen to be wetted, and such spontaneous wetting arises because wetting the hydrophilic patterned surface is energetically favorable compared to keeping the surface dry [37]. The interfacial energy change dE associated with advance of liquid by a distance dx through a groove and on top of a line pattern as illustrated in Fig. 4(a) is written as

$$dE = (\gamma_{SL} - \gamma_{SG})(s + w + 2h)dx + \gamma(s + w)dx, \tag{1}$$

where γ_{SL}, γ_{SG}, and γ are the solid-liquid, solid-gas, and liquid-gas interfacial energies, respectively. The first and second terms on the right-hand side (RHS) of Eq. (1) correspond to the energy change
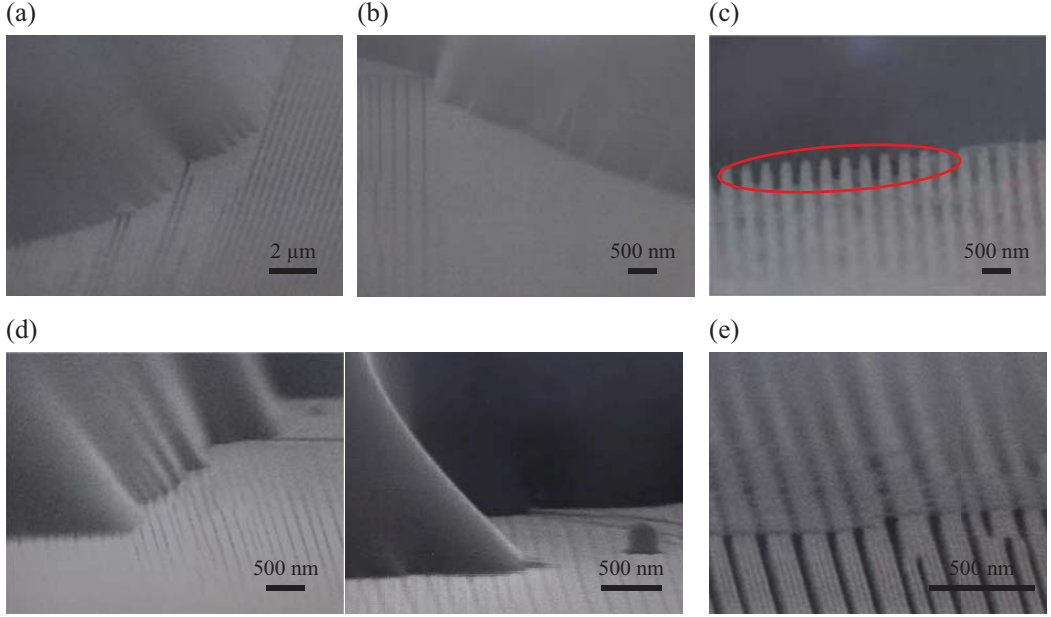
FIG. 3. (a) Expansion of water film when the water drop contacts the surface *LI*. (b) Expansion of water film when the water drop contacts the surface *SI*. (c) Wenzel state on the surface *LO*. (d) Cassie-Baxter state on the surface *SO*. (e) Nanoscopically thin water film left on surface *SO* after the drop has disappeared due to reduction of vapor pressure in the ESEM chamber.

due to wetting of the initially dry surface and that due to expansion of a liquid-gas interfacial area, respectively. Spontaneous liquid flow occurs when $dE/dx < 0$, which leads to

$$\frac{s+w}{2h} < \frac{\cos\theta}{1-\cos\theta},\tag{2}$$

where we used Young's equation $\gamma_{SG} - \gamma_{SL} = \gamma\cos\theta$, where θ is the equilibrium contact angle. The geometrical parameters of surfaces *LI* and *SI* satisfy Eq. (2) with θ taken to be the values on flat surfaces in Table I, which rationalizes the experimentally observed wicking behavior.
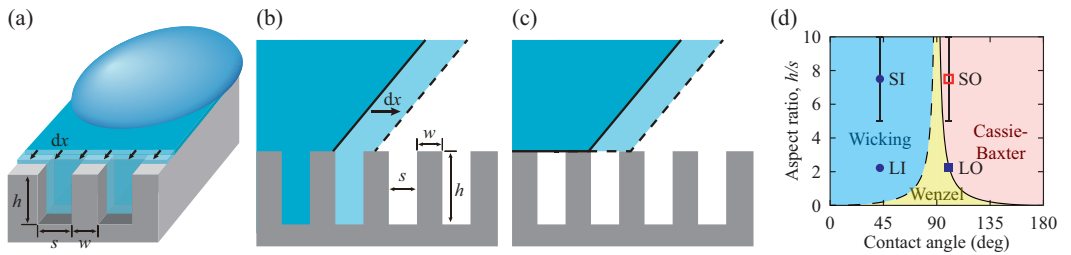

FIG. 4. (a) Schematic of the wicking of water through pattern gaps. (b) Schematic of the cross section of a liquid drop that invades gaps of a patterned solid surface. (c) Schematic of the cross section of a liquid drop that spreads over gaps of a patterned solid surface. (d) Regime map of the contact behavior of drops and solid patterns. The dashed line corresponds to $h/s = -(1 - 1/\cos\theta)/2$ and the solid line to $h/s = -(1 + 1/\cos\theta)/2$. The blue, yellow, and pink regions represent the spontaneous wicking, the Wenzel state, and the Cassie-Baxter state, respectively.

On the hydrophobic nanopatterns, wicking into the grooves surrounding the drop is absent as shown in Figs. 3(c) and 3(d). On the hydrophobic nanopatterns with a relatively large spacing, surface *LO*, the water invades the gaps just below the drop without wicking into the neighboring region [Fig. 3(c)]. The liquid within the nanogaps is clearly visible in the ellipse in the figure. Hence, the drop is in the Wenzel state on surface *LO*. However, when the gap spacing is finer (surface *SO*), the water does not fill the gap below the drop, as shown in Fig. 3(d). The drop is then in the Cassie-Baxter state. The absence of liquid within the nanogaps of surface *SO* is further evidenced by an image taken during the drying process in which the vapor pressure is reduced in the ESEM chamber [Fig. 3(e)]. The drop disappears with drying, leaving a footprint of nanoscopically thin water film. The film is so thin and transparent that the dry nanogaps below the footprint are seen, verifying the absence of liquid film in the gaps.

Whether or not a liquid drop will invade pattern gaps when touching a patterned surface depends on which state is energetically favorable. Figures 4(b) and 4(c) illustrate the cross section of a liquid drop on a patterned surface. When the liquid invades the gaps [Fig. 4(b)] the variation of interfacial energy caused by the displacement of the contact line dx is due to wetting of the initially dry solid surface (the first term on the RHS) and annihilation of the liquid-air interface (the second term on the RHS), written as

$$dE_1 = f(\gamma_{SL} - \gamma_{SG})dx + \gamma \, dx \cos\theta, \tag{3}$$

where $f = (s + w + 2h)/(s + w)$ is the surface roughness defined as the actual surface area to the projected area. When the liquid cannot invade the gaps [Fig. 4(c)] the variation of interfacial energy caused by the displacement of the contact line dx is written as

$$dE_2 = \phi(\gamma_{SL} - \gamma_{SG})dx + (1 - \phi)\gamma \, dx + \gamma \, dx \cos\theta, \tag{4}$$

where $\phi = w/(s + w)$ is the area density of the pattern tops. The first, second, and third terms on the RHS correspond to the energy change associated with the wetting of the initially dry pattern top surface, with the expansion of the liquid bottom exposed to the gas in the gap, and with the annihilation of the liquid-gas interfacial area, respectively.

We anticipate that the liquid tends to invade the pattern gaps when $dE_1 < dE_2$. Thus, the Wenzel state will be favored when $h/s < -(1 + 1/\cos\theta)/2$. The liquid cannot invade the pattern gaps when $dE_1 > dE_2$. Thus, the Cassie-Baxter state will arise when $h/s > -(1 + 1/\cos\theta)/2$. The aspect ratio, defined as the ratio of the pattern height to the gap spacing h/s, is 2.2 for surface *LO* and ranges from 5 to 10 for surface *SO*. We find the measured aspect ratios of *LO* and *SO* to satisfy the theoretical condition for the Wenzel state and the Cassie-Baxter state, respectively. Thus, our theory is consistent with the experimental observations.

Figure 4(d) summarizes our theoretical models to predict the contact behavior of drops and solid patterns and compares them with the experimental results. On hydrophilic substrates, the water tends to wick through gaps when $h/s > -(1 - 1/\cos\theta)/2$, which corresponds to relation (2) with $(s + w)$ replaced by s. Our experimental conditions for surfaces *LI* and *SI*, which exhibit spontaneous wicking, lie within the corresponding region colored blue in Fig. 4(d). The surface *LO* induces the Wenzel state experimentally, which is consistent with the theoretically predicted Wenzel region colored yellow. The Cassie-Baxter region colored pink in Fig. 4(d) includes the condition of surface *SO*.

V. CONCLUSION

We have shown that it is possible to observe the water meniscus formed on nanopatterned solid surfaces through ESEM by reducing the electron-beam heating of a viewing area. The liquid-state water has been brought onto the solid patterns by either vapor condensation or contact with an external water drop. Depending on the gap size between the nanowalls, the nanowall arrays were classified into types *L* (180 nm gap) and *S* (40–80 nm gap). By modifying the surface wettability, we obtained hydrophilic (*I*) and hydrophobic (*O*) patterns, so four kinds of solid patterns (*LI*, *SI*, *LO*,

and *SO*) were tested. Our observation results have allowed us to tell in which situations conventional microscale prediction still holds in nanoscales.

The condensation and wicking behaviors of hydrophilic nanopatterns *LI* and *SI* have been shown to differ little. Water is condensed in the grooves first and completely fills them, and a drop grows on top of the pattern tops. A liquid drop contacting hydrophilic patterns spreads on them by wicking into the grooves. However, the condensation and wicking behaviors of hydrophobic patterns *LO* and *SO* have been found to be different depending on the gap size. Water condenses sporadically in the gaps of surface *LO*, but it completely fills the gaps of surface *SO*. A water drop contacting surface *LO* assumes the Wenzel state by invading the pattern gaps below the drop, but it is in the Cassie-Baxter state on surface *SO*, failing to invade the gaps below the drop. A water drop resulting from condensation and an externally provided drop assume the same wetting state (Wenzel) on surface *LO*. However, on surface *SO*, the externally approached drop assumes the Cassie-Baxter state when contacting the solid pattern, while the condensed drop assumes the Wenzel state.

Our visualization results on hydrophilic nanopatterns are consistent with those that have been observed in microscales and predicted theoretically. We have shown that the wetting states of an external drop, which has been brought into contact with the solid patterns, either hydrophilic or hydrophobic, can be explained with a macroscopic model. However, the results of condensation experiments on hydrophobic nanopatterns defy our conventional (microscale) understanding associated with wetting. First, the early condensation of water in the grooves at RH less than 100% cannot be explained by a classical theory of capillary condensation, which predicts such early condensation for wettable surfaces. Second, the sporadic condensation in the grooves of surface *LO* and the complete wetting of the grooves of surface *SO* by condensed water can hardly be understood with the currently available wetting model. Although the theories of multilayer adsorption and capillary bridge formation appear to be related to what is observed on surfaces *SO* and *LO*, respectively, how the theories can be extended to hydrophobic surfaces is elusive. Third, it is very intriguing to see that water completely wets the narrow hydrophobic grooves of surface *SO* when condensing, although it cannot invade the gaps when an external drop contacts the same surface.

The behavior of a water meniscus on nanoscale patterns, which has not been visualized thus far, can extend our understanding of nanoscopic liquid wetting behavior. In the study of liquid meniscus dynamics, optical measurements have covered down to a few micrometers and computational approaches including molecular-dynamics simulation [38] and atomic-scale measurements using atomic force microscopy [22] have covered up to a few nanometers. Thus, the liquid behavior on the scales of tens to hundreds of nanometers has been rather elusive for the lack of adequate experimental observation techniques. We anticipate that our experimental results enabled by our delicate experimental technique can make substantial impact in advancing our knowledge of nanoscale wetting behavior.

ACKNOWLEDGMENTS

---

[1] T. D. Wheeler and A. D. Stroock, The transpiration of water at negative pressures in a synthetic tree, Nature (London) **455**, 208 (2008).

[2] X. M. Xu, G. Vereecke, C. Chen, G. Pourtois, S. Armini, N. Verellen, W.-K. Tsai, D.-W. Kim, E. Lee, C.-Y. Lin, P. Van Dorpe, H. Struyf, F. Holsteyns, V. Moshchalkov, J. Indekeu, and S. De Gendt, Capturing wetting states in nanopatterned silicon, ACS Nano **8**, 885 (2014).

[3] A. Lee, M.-W. Moon, H. Lim, W.-D. Kim, and H.-Y. Kim, Water harvest via dewing, Langmuir **28**, 10183 (2012).

[4] M. J. Kalmutzki, C. S. Diercks, and O. M. Yaghi, Metal-organic frameworks for water harvesting from air, Adv. Mater. 30, 1704304 (2018).

[5] A. LaPotin, H. Kim, S. R. Rao, and E. N. Wang, Adsorption-based atmospheric water harvesting: Impact of material and component properties on system-level performance, Acc. Chem. Res. 52, 1588 (2019).

[6] S. G. Lipson, H. Lipson, and D. S. Tannhauser, *Optical Physics*, 3rd ed. (Cambridge University Press, Cambridge, 1995).

[7] E. H. Synge, A suggested method for extending microscopic resolution into the ultra-microscopic region, Philos. Mag. 6, 356 (1928).

[8] E. A. Ash and G. Nicholls, Super-resolution aperture scanning microscope, Nature (London) 237, 510 (1972).

[9] D. W. Pohl, W. Denk, and M. Lanz, Optical stethoscopy: Image recording with resolution $\lambda/20$, Appl. Phys. Lett. 44, 651 (1984).

[10] E. Kim and G. M. Whitesides, Imbibition and flow of wetting liquids in noncircular capillaries, J. Phys. Chem. B 101, 855 (1997).

[11] P. Kim, H.-Y. Kim, J. K. Kim, G. Reiter, and K. Y. Suh, Multi-curvature liquid meniscus in a nanochannel: Evidence of interplay between intermolecular and surface forces, Lab Chip 9, 3255 (2009).

[12] A. H. Cannon and W. P. King, Visualizing contact line phenomena on microstructured superhydrophobic surfaces, J. Vac. Sci. Technol. B 28, L21 (2010).

[13] C. M. Megaridis, A. G. Yazicioglu, J. A. Libera, and Y. Gogotsi, Attoliter fluid experiments in individual closed-end carbon nanotubes: Liquid film and fluid interface dynamics, Phys. Fluids 14, L5 (2002).

[14] M. P. Rossi, H. Ye, Y. Gogotsi, S. Babu, P. Ndungu, and J.-C. Bradley, Environmental scanning electron microscopy study of water in carbon nanopipes, Nano Lett. 4, 989 (2004).

[15] U. M. Mirsaidov, H. Zheng, D. Bhattacharya, Y. Casana, and P. Matsudaira, Direct observation of stick-slip movements of water nanodroplets induced by an electron beam, Proc. Natl. Acad. Sci. USA 109, 7187 (2012).

[16] K. K. Varanasi, M. Hsu, N. Bhate, W. Yang, and T. Deng, Spatial control in the heterogeneous nucleation of water, Appl. Phys. Lett. 95, 094101 (2009).

[17] S. Anand, A. T. Paxson, R. Dhiman, J. D. Smith, and K. K. Varanasi, Enhanced condensation on lubricant-impregnated nanotextured surfaces, ACS Nano 6, 10122 (2012).

[18] K. Rykaczewski, J. H. J. Scott, and A. G. Fedorov, Electron beam heating effects during environmental scanning electron microscopy imaging of water condensation on superhydrophobic surfaces, Appl. Phys. Lett. 98, 093106 (2011).

[19] K. Rykaczewski and J. H. J. Scott, Methodology for imaging nano-to-microscale water condensation dynamics on complex nanostructures, ACS Nano 5, 5962 (2011).

[20] S. Rozhok, P. Sun, R. Piner, M. Lieberman, and C. A. Mirkin, AFM study of water meniscus formation between an AFM tip and NaCl substrate, J. Phys. Chem. B 108, 7814 (2004).

[21] D. Lohse and X. Zhang, Surface nanobubbles and nanodroplets, Rev. Mod. Phys. 87, 981 (2015).

[22] M. V. Vitorino, A. Vieira, C. A. Marques, and M. S. Rodrigues, Direct measurement of the capillary condensation time of a water nanobridge, Sci. Rep. 8, 13848 (2018).

[23] K. Singh, J. R. Lister, and D. Vella, A fluid-mechanical model of elastocapillary coalescence, J. Fluid Mech. 745, 621 (2014).

[24] T.-H. Kim, J. Kim, and H.-Y. Kim, Evaporation-driven clustering of microscale pillars and lamellae, Phys. Fluids 28, 022003 (2016).

[25] B. L. Weeks and M. W. Vaughn, Direct imaging of meniscus formation in atomic force microscopy using environmental scanning electron microscopy, Langmuir 21, 8096 (2005).

[26] J. W. van Honschoten, N. Brunets, and N. R. Tas, Capillarity at the nanoscale, Chem. Soc. Rev. 39, 1096 (2010).

[27] T. Hofmann, M. Tasinkevych, A. Checco, E. Dobisz, S. Dietrich, and B. M. Ocko, Wetting of Nanopatterned Grooved Surfaces, Phys. Rev. Lett. 104, 106102 (2010).

[28] D. Quéré, Rough ideas on wetting, Physica A 313, 32 (2002).

[29] Y. C. Jung and B. Bhushan, Wetting behaviour during evaporation and condensation of water microdroplets on superhydrophobic patterned surfaces, J. Microsc. 229, 127 (2008).

[30] N. Miljkovic, R. Enright, and E. N. Wang, Modeling and optimization of superhydrophobic condensation, ASME J. Heat Transfer **135**, 111004 (2013).

[31] R. M. Pashley, Multilayer adsorption of water on silica: an analysis of experimental results, J. Colloid Interface Sci. **78**, 246 (1980).

[32] J. Li, X. Li, K. Wu, D. Feng, T. Zhang, and Y. Zhang, Thickness and stability of water film confined inside nanoslits and nanocapilliaries of shale and clay, Int. J. Coal Geol. **179**, 253 (2017).

[33] R. Evans, U. M. B. Marconi, and P. Tarazona, Fluids in narrow pores: Adsorption, capillary condensation, and critical points, J. Chem. Phys. **84**, 2376 (1986).

[34] A. Carlson, P. Kim, G. Amberg, and H. A. Stone, Short and long time drop dynamics on lubricated substrates, Europhys. Lett. **104**, 34008 (2013).

[35] V. M. Starov and M. G. Velarde, Surface forces and wetting phenomena, J. Phys.: Condens. Matter **21**, 464121 (2009).

[36] V. Starov, Static contact angle hysteresis on smooth, homogeneous solid substrates, Colloid Polym. Sci. **291**, 261 (2013).

[37] J. Kim, M.-W. Moon, and H.-Y. Kim, Dynamics of hemiwicking, J. Fluid Mech. **800**, 57 (2016).

[38] O. Beckstein and M. S. P. Sansom, Liquid-vapor oscillations of water in hydrophobic nanopores, Proc. Natl. Acad. Sci. USA **100**, 7063 (2003).